

Article

Density Functional Investigation of [001] and [111] SiNWs and the Effect of Doping with Boron and Phosphorus

Nedhal Ali Mahmood Al-Nuaimi *, Florian Hilser and Sibylle Gemming 

Theoretical Physics of Quantum Mechanical Processes and Systems, Institute of Physics, Chemnitz University of Technology, D-09107 Chemnitz, Germany

* Correspondence: nedhal-ali-mahmood.al-nuaimi@physik.tu-chemnitz.de; Tel.: +49-371-531-37077

Abstract: In the present study, we investigate the influence of boron (B) and phosphorus (P) (p- and n-type, respectively) doping on the electronic properties of ultra-thin silicon nanowires (SiNWs) by gradient-corrected density functional calculations with the Perdew–Burke–Ernzerhof (PBE) approximation. In the limit of very small diameters (5–8 Å), both pristine and highly active unsaturated SiNWs with orientations along the [001] and [111] directions exhibit electronic states around the Fermi level, indicative of conductive properties. Conduction is further enhanced by the introduction of doping atoms, as demonstrated by the relative change in the band structures of SiNWs with and without B and P doping. This investigation provides an important insight into the electronic states of SiNWs, which are candidates for future electronics or sensing applications.

Keywords: Si nanowire; doping; ABINIT; simulation; band structure



Citation: Al-Nuaimi, N.A.M.; Hilser, F.; Gemming, S. Density Functional Investigation of [001] and [111] SiNWs and the Effect of Doping with Boron and Phosphorus. *Crystals* **2024**, *14*, 585. <https://doi.org/10.3390/cryst14070585>

Academic Editor: Francisco M. Morales

Received: 30 April 2024

Revised: 13 June 2024

Accepted: 20 June 2024

Published: 25 June 2024



Copyright: © 2024 by the authors. Licensee MDPI, Basel, Switzerland. This article is an open access article distributed under the terms and conditions of the Creative Commons Attribution (CC BY) license (<https://creativecommons.org/licenses/by/4.0/>).

1. Introduction

Recent advances in the experimental investigation of silicon nanowires (SiNWs) have paved the way to a manifold of formation techniques and to the use of SiNWs in a multitude of applications, which range from electronic sensing, even down to the attomolar regime over employing the high surface-to-volume ratio for energy storage in batteries to energy harvesting in thermoelectric devices [1–5]. The journey from understanding the physics of how nanowires work to finding practical uses for them has led to many benefits for the wider research community in materials, chemistry, and engineering.

To name the most advanced fields, silicon-based nanostructures have been widely studied in the past 30 years as potential candidates for transistors [6–8], tunneling diodes [9], biological sensors [1,10–16], catalysts [17,18], and even quantum computer hardware [19], which have contributed to many new applications. Controlling the electronic properties of nanostructures [20] is critical when developing these applications.

One of the most studied aspects of SiNWs, which relies on the first-principles formalism, regards their structure-dependent electronic properties, particularly the dependency of the electronic states on the diameters and crystallographic orientations. For example, it has been observed that the electronic and optical properties of silicon nanowires (SiNWs) are highly sensitive to particular crystalline orientations, which lead to different band folding along the wire and to different quantum confinement with respect to the diameter [21].

This is evidenced by Svizhenko [22] and coworkers, who showed using tight binding modeling, that the band structure has a significant effect on the transport properties of SiNWs along different crystallographic directions. Similarly, Neophytou [23] and coworkers showed that the valence and conduction band splitting caused by the gate voltage affects the conductivity of wires in different orientations with variations of several orders of magnitude. Numerically demanding first-principles calculations on the electronic properties of SiNW devices with diameters above 10 nm exhibited physical properties that did not strongly depend on material sizes due to the lack of quantum confinement [24].

Fuchs et al. [25] provided a generalized gradient-corrected DFT study with the Tran and Blaha [26] mGGA potential and to determine the band gaps of SiNWs with different diameters and orientations. They observed that the density of states was highest at the SiNW center and decayed towards the surface, leading to more localized electron transport than hole transport. For SiNWs, the transport channels spatially followed zigzag-shaped silicon chains along the wire, while being transported radially, and the transport was limited by the band gap increase towards the wire surface. Therefore, SiNWs with relatively small diameters revealed anisotropic emerging electronic properties; these are quite interesting, given the industrial need for device miniaturization and the strong correlation between physical properties and sample sizes [25]. Specifically, this finding was in line with the synthesis of ultra-thin [001] SiNWs with diameters between 1.3 nm to 7 nm via an oxide-assisted growth method, in which SiO powder was heated to 1200 °C in an alumina tube by Ma et al. [27] or with transport measurements on SiNWs created along the [100], [111], or [110] directions [28].

Holmes et al. [29] synthesized SiNWs with diameters of 4 to 5 nm in both a [100] and [110] orientation by thermally degrading diphenylsilane in sc-hexane (supercritical temperature $T_c = 235$ °C and pressure $P_c = 530$ bar) at 500 °C and 200 or 270 bar in an inconnell high-pressure cell. Wu et al. [30] grew [110], [111], and [112] SiNWs down to 3 nm in diameter, by chemical vapor deposition (CVD) using gold nano-clusters as the catalysts and silane (SiH_4) as a vapor-phase reactant.

The diverse array of established synthesis methods for SiNW growth, such as CVD and solution-based techniques, coupled with the well-documented growth mechanisms—vapor-liquid-solid (VLS), vapor-solid-solid (VSS), and solution-liquid-solid (SLS)—facilitates the widespread fabrication of SiNWs. Theoretical studies using ABINIT software, which employs density functional theory (DFT) and ab initio molecular dynamics, provided deep insights into the electronic structure and mechanical properties of Si NWs. The theoretical findings align well with the experimental data, enhancing the understanding of solid electrolyte interphase (SEI) formation and the dynamics of alloying and dealloying processes, making them suitable for various operando analytical techniques [31–34].

Moreover, controlling doping is essential for semiconducting device manufacturing, as the corresponding band gap changes drastically with the doping concentration and its relative distribution [35–40]. Common doping schemes for very thin nanowires employ the modulation of the electrostatic potential provided by a passivating SiO_2 or hBN shell around SiNWs by including additional ions such as Al^{3+} or Mg^{2+} [41,42]. This route prevents strong local composition changes inside the wire, which may become crucial in ultra-thin semiconductor wires, as the electronic properties of SiNWs could then be controlled by the presence of dopants acting as impurities. However, modulation doping is only possible in the presence of an encapsulation shell, which may, in turn, reduce the sensing capability of the wire. Hence, the present simulation addresses this aspect by employing structure models from pure silicon without further passivation as a starting point for potential targeted surface functionalization. Earlier DFT studies on Germanium nanowires suggest that both dopant and surface states bear the potential to modify and tune the sensing potential of semiconductor nanowires [43]. Similar DFT studies investigated the properties of ultra-thin, hydrogen-passivated SiNWs oriented along the [001] direction, their doping with boron, their interaction with molecules and the modification of their properties by the presence of adsorbates [44].

DFT calculations reveal the stability of nano-wires made of endohedral MSi_{12} cage-like molecules, especially with light transition metals ($M = \text{Fe}, \text{Ni}, \text{Co}, \text{Ti}, \text{V}, \text{and Cu}$). These nano-wires, stabilized by metal atoms along their axes, resemble Si-based versions of carbon nanotubes with hexagonal cross-sections. Regardless of the metal, longer nano-wires exhibit decreasing HOMO–LUMO gaps, suggesting metallic behavior suitable for self-assembled nano-devices [45].

Oliveira et al. theoretically determined the static dipole polarizabilities and optical response of M@Si_{12} ($M = \text{Ti}, \text{Cr}, \text{Zr}, \text{Mo}, \text{Ru}, \text{Pd}, \text{Hf}, \text{and Os}$) and M@Si_{16} ($M = \text{Ti}, \text{Zr}, \text{and Hf}$)

clusters using ab initio plane-wave DFT calculations. The optical gaps were calculated with the frequency-dependent GW approximation, allowing for efficient treatment of d and f orbitals with a low computational cost. The results showed that Ti@Si12, Cr@Si12, Zr@Si12, Mo@Si12, Ru@Si12, Pd@Si12, Hf@Si12, and Os@Si12 clusters were semiconducting with large energy gaps, influenced by caging effects and the size of the encapsulated metal atom. Additionally, M@Si16 clusters exhibited enhanced electronic stability and similar HOMO-LUMO gaps compared with M@Si12 clusters, suggesting potential applications in tunable optoelectronic nanodevices [46].

In the present study, the electronic properties of both [001] and [111] oriented ultra-thin pristine SiNWs are investigated via first-principles calculations, and the influence of doping by boron (B) or phosphorus (P) atoms on the electronic properties will be analyzed.

2. Model Systems

All nanowire structures, pristine SiNWs oriented along the [001] and [111] directions, and their B and P-doped analogues were built using the software VESTA [47]. Initially, we started with a primitive unit cell of bulk silicon (Si), as published in the American Mineralogist database [48]. The optimized structure represented the building block, from which we constructed well-defined (oriented) SiNW supercells either by exposing the (001) or (111) plane. That step was followed by constructing the nanowires in the desired direction, which was oriented along the Z axis, and periodic boundary conditions were applied in all three spatial directions. A vacuum space of 15 Å was added in both X and Y directions to ensure that the model structures represented truly one-dimensional SiNWs. This vacuum space was large enough to eliminate the interactions between the nanowire and its periodic replicas in the adjacent simulation cells. For the [001] SiNW, the repeated structural unit contained 13 atoms, while in the case of [111] SiNWs, there were 22 atoms in the supercell. To investigate the effect of doping, we replaced one silicon atom with either one B or P atom and we investigated the symmetrically inequivalent positions separately.

In the present investigation, the atom positions of the bulk-derived starting structures for the pristine SiNWs were structurally relaxed according to the forces obtained from first-principles employing gradient-corrected density-functional band-structure calculations. Those relaxed pristine structures served as starting points for the further optimization of B- and P-doped SiNWs. The so-obtained atom configurations were the stable minima of the total energy hypersurface; despite the relaxations, they still exhibited the same local coordination of the constituent atoms along the wire direction as the starting structures. The resulting structures are depicted in Figure 1 for the [001] direction and in Figure 2 for [111].

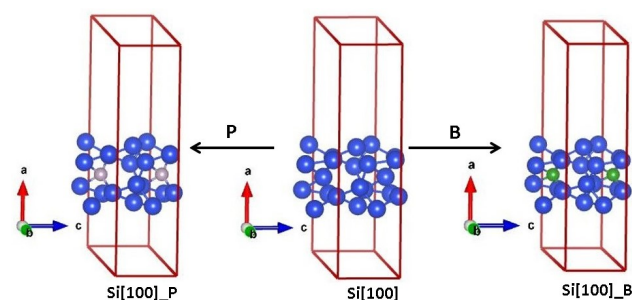


Figure 1. The atomic structure of: SiNWs[001] with P, SiNWs[001], and SiNWs[001] with B; Si atoms are shown in blue, B atoms in green, and P atoms in grey.

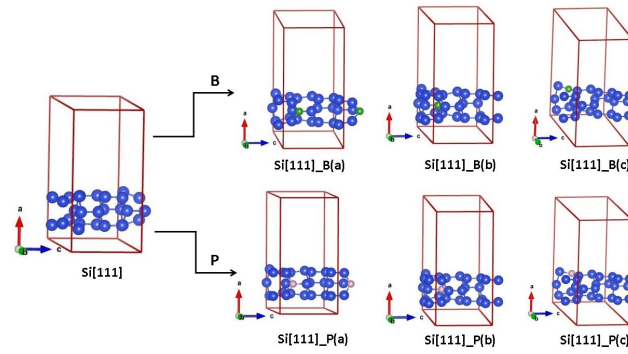


Figure 2. Atomic structure of SiNWs[111], SiNWs[111] with B, and SiNWs[111] P in positions a, b, and c. Si atoms are shown in blue, B atoms in green, and P atoms in grey. a, b, and c denote the substitution of dopant at three different positions on SiNWs[111] structures.

We emphasize that the present investigation with the respective small number of atoms reflects only the very core of potential nanowires that can be realized in experiments, due to the lack of technical capabilities of building and stabilizing a similar miniature structure without further embedding. Nevertheless, the study may be generalized to investigate nanowires with larger diameters and different types of coupling to a passivation shell.

3. Quantum Computational Methods

3.1. Total Energy Method

Solving the Schrödinger equation for many-body systems enabled us to obtain many properties of a system composed of N -interacting electrons in the external potential of the nuclei. The equation of the Hamiltonian is given as:

$$\hat{H}\psi(\vec{r}_1, \dots, \vec{r}_{N_{el}}) = E\psi(\vec{r}_1, \dots, \vec{r}_{N_{el}}) \quad (1)$$

In this context, the Hamilton operator can be written as:

$$\hat{H} = -\sum_i^{N_{el}} \frac{\hbar^2}{2m_e} \Delta_i + \sum_i^{N_{el}} V_{ext}(\vec{r}_i) + \frac{e^2}{2} \sum_{i \neq j}^{N_{el}} \frac{1}{|\vec{r}_i - \vec{r}_j|} \quad (2)$$

where \vec{r}_i represents the coordinates of electron i , Δ_i denotes the Laplacian operator with respect to the coordinate \vec{r}_i , while $V_{ext}(\vec{r}_i)$ refers to the external potential acting on the electrons and is parametrically dependent on the nuclear positions. To obtain a numerical solution for the Schrödinger Equation (1), it is necessary to use an efficient electronic structure method. One such method is DFT, based on the seminal works by Hohenberg and Kohn, and Kohn and Sham [49,50].

This approach establishes a direct relationship between the electronic charge density $\rho(\vec{r})$ in the ground state and the external potential $V_{ext}(\vec{r})$. Therefore, as the many-body wave-function of the ground state is also determined by the external potential, all physical properties of the system in this state can be described as a functional of the electronic charge density. In particular, the total energy of the ground state plays a significant role in determining various characteristics of the system, and can be expressed as an expectation value of the Hamiltonian on its wave-function Ψ_0 . By utilizing this approach, we can express the total energy as a functional of the electronic density [49,50].

$$E[\rho(\vec{r})] = \langle \Psi_0 | \hat{H} | \Psi_0 \rangle = F[\rho(\vec{r})] + \int_V V_{ext}(\vec{r})\rho(\vec{r})d^3r \quad (3)$$

In Equation (3), the integral is evaluated across the entire volume V of the system, where $F[r]$ is a universal functional of the density determined by the ground state's expectation values for kinetic energy and electrostatic electron repulsion terms. The functional

$E[\rho(r)]$ is minimized with regards to the electronic density, under the condition that the number of electrons N_{el} remains constant.

$$\int_V \rho(\vec{r}) d^3r = N_{el} \quad (4)$$

This gives the ground-state total energy and the electronic density. Kohn and Sham (KS) [50] proposed a novel functional that transforms the many-body problem into a problem of non-interacting electrons while maintaining the ground-state electronic density, as the specific form of the universal functional $F[\rho(\vec{r})]$ remains unknown. This new functional can be derived by reformulating the second term in Equation (3) as shown in [49,50].

$$F[\rho(\vec{r})] = T_0[\rho(\vec{r})] + E_H + E_{xc}[\rho(\vec{r})] \quad (5)$$

where, the total energy of a system of non-interacting electrons is composed of three terms. The first term represents the kinetic energy; the second term takes into account the classical Coulomb interaction between a spatial charge distribution $\rho(r)$; and the third term accounts for the exchange-correlation energy [49,50], with its functional from being unknown. Therefore, in solving the many-body problem, the accuracy will ultimately depend on the quality of this approximation. Upon substituting this new functional expression, the total energy in Equation (3) is now:

$$E[\rho(\vec{r})] = \langle \Psi_0 | \hat{H} | \Psi_0 \rangle = T_0[\rho(\vec{r})] + E_H + E_{xc}[\rho(\vec{r})] + \int_V V_{ext}(\vec{r})\rho(\vec{r})d^3r \quad (6)$$

Using this approach, the structural, energetic, and electronic properties of silicon nanowires and those influenced by substitutional B and P atoms are calculated here from first principles.

3.2. Computational Methods

All nanowires in the present study were simulated using first-principles total energy electronic structure calculations based on the DFT, as implemented in the program package ABINIT [51].

In accordance with prior calculations on conducting silicon nanowires (e.g., in refs. [17,52–54]), the generalized gradient approximation (GGA) in the parametrisation by Perdew, Burke, and Ernzerhof (PBE) [55] was employed, which also served as a reference functional for round-robin tests of density-functional implementations, because it provides a good overall representation of the structural and electronic features of crystalline materials and nanostructures [56]. Compared with functionals such as revised PBE versions that were specifically parameterized to experimental adsorption energies [57,58], the standard PBE functional has been observed to yield, in particular, structural properties in better agreement with data from experiment and from high-level ab initio calculations [58]. A cutoff energy of 20 Ha was applied for bulk silicon (Si) and nanowires, along with Monkhorst–Pack k-point grids ($6 \times 6 \times 6$) for bulk Si in the standard cubic cell and ($1 \times 1 \times 8$) for SiNWs to ensure the convergence of the total energy within 10^{-6} Ha per atom. In the geometry optimizations, all atomic positions are fully relaxed until the absolute value of force acting on each atom is less than 5×10^{-6} eV/Å.

To describe the interaction between the ionic cores and the valence electrons, norm-conserving pseudopotentials were used; those pseudopotentials were generated with the PBE functional for the atom configurations Si $[1s^2 2s^2 2p^6] 3s^2 3p^2$, B $[1s^2] 2s^2 2p^1$, and P $[1s^2 2s^2 2p^6] 3s^2 3p^3$, as provided by the abinit repository [59]. Even though very thin, SiNWs exhibited a band dispersion along the wire direction, which is calculated by finding the energy eigenvalues of the total Hamiltonian with respect to the k_z vector. The corresponding results are shown in the following section.

4. Results And Discussion

4.1. Structural Properties

All atomic positions and lattice parameters of bulk silicon (Si), pristine SiNWs [001], and SiNWs [111], and the doped ones with B and P, were completely relaxed (optimized) by minimizing the total energy and atomic forces. However, the relaxation of the nanowire along its central axis was the most significant as it determined the band structure. Figures 1 and 2 display the atomic structures of the two nanowire types after the optimization. The fundamental difference between the two wires is given by the arrangement of the Si sp^3 hybrid bonds with respect to the direction of the orientation along the wire. The resulting specific connectivity of the silicon atoms and their surroundings and the alignment with the wire direction create a unique local structure that has been shown to correlate with the charge conductance channels within thicker wires [25]. The equilibrium lattice constant (a_0) for Si was obtained and compared with the literature, as shown in Table 1. It was used as a reference to discuss the structural features of the nanowires, in particular the periodicity along the wires.

Table 1. The calculated equilibrium lattice constant (a_0) and band gaps (Δg) of bulk silicon. Theoretical and experimental values are provided for comparison.

	a_0	Ref.		Δg	Ref.
GGA	5.46	our work	GGA	0.607	our work
LDA	5.41	[60]	BLYP	1.39	[6]
LDA	5.4	[61]	PW91PW91	1.13	[6]
LDA	5.38	[62]	BPW91	1.15	[6]
PBE	5.47	[63]	BPBE	1.13	[6]
Exp.	5.43	[64]	B3LYP	2.02	[6]
			LSDA	0.95	[6]
			GGA	0.59	[6]
			Exp.	~ 1.17	[65]

As shown in Table 1, our value of a_0 for the Si bulk was compatible with the values obtained by both experimental and theoretical studies with the same and similar exchange and correlation functionals. For further correlation of the structural and electronic features, the valence electron density of the SiNW, as calculated by the ABINIT code, was analyzed by the cut3d utility, which forms part of the ABINIT distribution. Cut3d utilizes a trilinear interpolation technique to calculate the density, using a Fast Fourier Transform (FFT) to divide the space into small rectangular parallelepipeds. Moreover, cut3d enables data interpolation along a line, enabling us to obtain the density, density gradient, and density Laplacian along a specified line. This method improves the precision and effectiveness of generating a spatially well resolved representation of the density files produced. Thus, we obtained the density for the optimum lattice constants of the oriented SiNWs[001], [111], and the doped ones, as shown in Table 2.

From the table, we note that along the c axis, which is the wire direction, all silicon nanowires exhibited a slightly reduced lattice spacing compared with the bulk silicon as a result of confinement effects and surface interactions within the nanowire structure [66]. In accordance with the bulk crystalline lattice, the optimized repeat unit along [111] was nearly $\sqrt{3}$ times as large as the one found for the [001] wire. Reflecting the four-fold symmetry of the $\langle 001 \rangle$ direction of pure silicon, even the ultra-thin, pure [001] wire maintained a square cross-section geometry. Similarly, the cross-section of the [111] wire exhibited an $a:b$ ratio of approximately $1:\sqrt{3}$; hence the pure wires were structurally rather close to the bulk crystal.

Table 2. Lattice constants of SiNWs[001] and SiNWs[111] doped with B and P.

	Lattice Constants		
	a (Å)	b (Å)	c (Å)
SiNWs[001]	20.43	20.43	5.43
SiNWs[001]-B	20.43	20.43	5.43
SiNWs[001]-P	20.43	20.43	5.43
SiNWs[111]	18.84	21.65	9.40
SiNWs[111]-B(a)	18.84	21.65	9.40
SiNWs[111]-B(b)	18.84	21.65	9.40
SiNWs[111]-B(c)	18.84	21.65	9.40
SiNWs[111]-P(a)	18.84	21.65	9.40
SiNWs[111]-P(b)	18.84	21.65	9.40
SiNWs[111]-P(c)	18.84	21.65	9.40

Yet, already tiny discrepancies in interatomic distances may result in alterations of the physical and electronic characteristics of silicon nanowires in contrast with bulk silicon already for the pristine wires, which may be exploited for sensing. Even stronger changes in the local coordination were obtained when doping the wire substitutionally with heteroatoms. In particular, the introduction of a dopant with an ionic radius different from that of the host atoms locally leads to strong lattice expansion or contraction [67]. Here, the ultra-thin wire geometry has the advantage of also stabilising very small or large dopant atoms, because such strains can be accommodated locally by radial relaxation, and no long-range lattice deformations occur, which would hamper doping the 3D extended bulk phase. To study the influence of the atomic radius, we chose P as a dopant atom from the same row of the periodic table as Si, and compared the influence on the local bonding environment with the considerably smaller B atom. Full geometry relaxation of all of the investigated structures led to the stable wire geometries depicted in Figures 1 and 2. For the three different doping sites in the $\langle 111 \rangle$ wires, the small B dopant favoured the position in the center of the wire, whereas the larger P atom found its most stable position at the wire surface. Extrapolating this observation to thicker Si nanowires, this implies that radial doping profiles with B in the center and P at the surface or interface to a passivating oxide or nitride coating would be favoured over doping subsequent segments, and that the latter device geometry may experience a thermodynamic driving force towards interdiffusion of the dopants at the interfaces between the segments.

In detail, Table 3 summarises the local bond lengths in the first coordination shell around B and P dopants with respect to the corresponding pure Si wire for all of the investigated structures. The strongest local structure changes were observed for the highly coordinated dopant positions in the centre of the wires, followed by the undercoordinated position on the wire surface. Substitutional B doping unequivocally led to a significant reduction in bond lengths by 15% to 24%. In contrast, the local bond length changes for P varied by a smaller amount, and amounted to reductions by 2% to 7%. In addition, for P, two outliers with considerable expansions of up to 18% occurred for the central position of the [001] wire, where the local coordination sphere around P tended to be four-fold with slightly reduced Si-P distances instead of the six-fold one in the pristine Si and the B-doped nanowires. The structural trends observed here reflect the changes obtained recently by Guo et al. [18] in a study on nitrogen activation by thin, pristine, and surface-doped hydrogen-terminated SiNW with the RPBE functional: For boron as the surface dopant, a significant reduction in bond lengths in the environment and a concomitant local reduction in the diameter was found, whereas for phosphorus, the local structure changes were minor and tended towards the longer side [18].

As an overall trend, already the coordination environment in both pristine nanowires exhibited a reduced symmetry, which resulted from the slight longitudinal contraction of the supercell along the c direction and the concomitant radial expansion of the bond

lengths by 1% to 4% with respect to the pristine bulk Si. This effect was enhanced by both dopants, but in different manners: for the [001] wire, the radial structure change reflected mostly the size effect of the dopant and maintained the two-fold symmetric distortion of the pristine wire, whereas the three-fold symmetry of the [111] wire was reduced to a two-fold one upon doping the center position (a) and was completely broken for the positions (b) and (c). Such symmetry changes also led to modifications of the electronic structure and conductivity of the nanowires compared with the bulk phase, which may be exploited for sensing local changes of the electrostatic potential of the environment and will be analyzed in the following.

Table 3. Bond lengths around the dopant sites of SiNWs [001] and SiNWs[111] with B or P dopants.

	Bond Lengths					
	$d_1/\text{Å}$	$d_2/\text{Å}$	$d_3/\text{Å}$	$d_4/\text{Å}$	$d_5/\text{Å}$	$d_6/\text{Å}$
SiNWs[001]	2.430	2.457	2.463	2.381	2.381	2.452
SiNWs[001]-B	2.101	2.117	2.118	2.046	2.046	2.108
SiNWs[001]-P	2.796	2.951	2.406	2.271	2.271	2.364
SiNWs[111]	2.397	2.397	2.410	2.464	-	-
SiNWs[111]-B(a)	1.957	1.957	1.954	2.106	-	-
SiNWs[111]-B(b)	2.031	2.054	2.054	2.065	-	-
SiNWs[111]-B(c)	1.890	1.910	-	-	-	-
SiNWs[111]-P(a)	2.237	2.237	2.259	2.288	-	-
SiNWs[111]-P(b)	2.317	2.317	2.294	2.302	-	-
SiNWs[111]-P(c)	2.189	2.200	-	-	-	-

4.2. Band Structures of Bulk Si, Undoped SiNWs, and Doped SiNWs

The band structure as a fundamental concept in solid-state physics provides the electronic energy levels in infinitely extended, ideal periodic crystal structures. For the nanowire models studied here, this periodicity was maintained in the z direction, whereas the structures were confined in x and y directions, confining the electron in those two directions. As the nanowires were oriented along the z direction, the energy levels were specified by two quantum numbers: the Bloch vector k_z and the band index n . The general features of the bands of all nanowires could be analyzed by comparing them with the band structure of bulk Si. Experimentally, bulk Si is an indirect band gap semiconductor that has a band gap of 1.17 eV, making it suitable for constructing micro-electronic devices such as field effect transistors (FETs) [68].

As depicted in Figure 3, the band gap of bulk silicon was determined by DFT-GGA calculations as the energy difference between the highest occupied state at the top of the valence band and the lowest occupied state at the bottom of the conduction band is 0.607 eV.

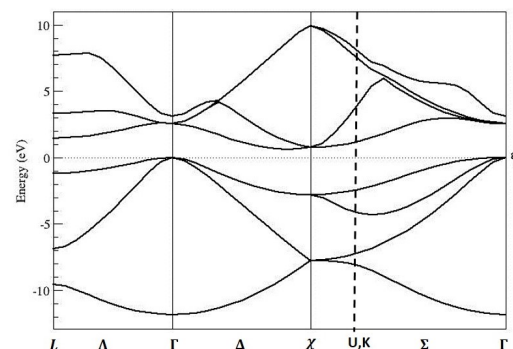


Figure 3. Band structure of bulk silicon.

Our band gap (Δg) value was in good agreement with the value obtained by GGA (in ref. [63]) and exhibited the previously established deviations from other theoretical and experimental values, as presented in Table 1. The outline in ref. [6] (see Table 1) highlights

that the BLYP and B3LYP exchange and correlation functionals overestimated the band gap, while the LSDA and the GGA methods underestimated it. Similar results have been obtained using a structure optimized with the semi-empirical AM1 method.

We tested the meta GGA functional by Tran and Blaha [26] for pure, H-passivated SiNWs [25] and found an improvement in the gap upon slight tuning of the addition parameters. For SiGe alloys, we experienced a stronger need for reparameterization. Therefore, we preferred not using the Tran–Blaha functional for the present case, where we had no reference for the doped wires.

In the following, the main changes to the band structure of undoped [001] and [111] SiNWs and the doped ones with B and P are discussed in detail. After converging the atomic positions of [001] and [111] SiNWs, we calculated the electronic band structures at an electronic temperature approaching zero.

Generally speaking, SiNWs grown experimentally exhibit facets, where the silicon coordination deviates from the highly directional covalent bonds following the sp^3 tetrahedral hybridization pattern. On unpassivated flat surfaces as well as flat facets of nanostructures, Si atoms at the surface have dangling bonds, which are unsaturated, make the atom highly active with respect to its chemical and physical environment, and may induce strong reconstruction of the surfaces. Surface passivation can be achieved with elements or compounds such as hydrogen, hydroxyl groups, or glassy oxides, which assure the chemical stability of the surface, but maintain or tune the sensitivity of the underlying pristine Si backbone [69]. However, the exploration of surface physics in these low-dimensional systems without passivation is highly intriguing due to the intricate interplay between an unusually high surface-to-bulk ratio and the impact of quantum confinement. Thus, we focussed on this Si backbone, here, and investigated its direct doping.

In this work, 21 k -points were selected from Γ to z , with Γ representing the 1st k -point and z representing the 21st k -point within band structures. The results are shown in Figure 4 in the absence of surface passivation such as hydrogen or hydroxyl groups. Such a pristine SiNW [001] backbone exhibited a metallic behavior with either zero or an extremely small negative band gap.

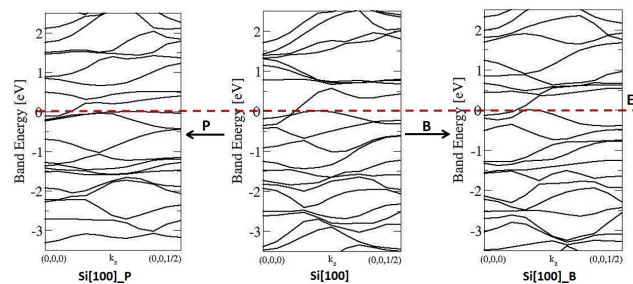


Figure 4. Band structures of [001] SiNWs doped with P, [001] SiNWs, and [001] SiNWs doped with B.

The result demonstrates that pristine SiNWs [001] can be good conductors. As discussed above, the absence of passivation leads to a strong reconstruction of the local bonding environment [001] SiNWs, resulting in the wire acquiring metallic properties [70].

As observed in earlier DFT studies on pristine and doped hydrogen-terminated SiNWs, the adsorption of small molecules on the wire-surface-induced localised states [18,54], which do not strongly overlap with the dispersing bands of SiNW. Providing such localised states in the absence of passivation may increase the binding propensity of the presently studied wires and modify the electronic structure of SiNW more strongly. The metallicity to be exploited here, has been observed for [001] SiNWs already previously via DFT calculation within the GW approximation [71].

As the new tuning approach, substitution doping of [001] SiNWs by B and P is introduced, as depicted in Figure 4. In semiconductor physics, doping typically refers to a minute concentration of impurities introduced into the crystal either by substitution or interstitially with an average nearest neighbor distance of several lattice parameters [72]. For ultra-thin

wires, these concentration limits may be exceeded. Hence, SiNW conductance has alternatively been adjusted by applying a gate voltage in a reconfiguration SiNW FET [73].

In our case of SiNWs doped centrally with B and P, the presence of either donor or acceptor states can considerably lower the energy gap of the pristine [001] SiNWs; thus, doping may considerably affect the electrical properties of SiNWs. In the case of [001] SiNWs that were doped with B, the conductivity can be increased through an extra charge carrier in the form of holes in the valence band, which improves the conductivity of the nanowire. For P-doped [001] SiNWs, the conduction band contains extra electrons, which increase the carrier concentration at the Fermi level and improve the electrical conductivity.

Experimental measurement of the conductance of thin SiNWs after annealing showed a much higher conductivity than the one expected from doping [74].

In contrast, band folding for [111] SiNWs led to a tiny direct gap at $k_z = (0,0,1/4)$, as shown in Table 4 and Figures 5 and 6. This direct nature can be attributed to symmetry breaking and quantum confinement effects, which both lead to the modification of the band structure [75].

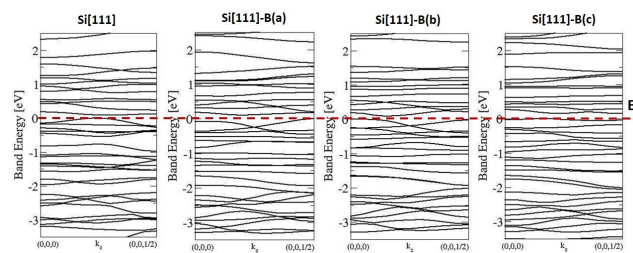


Figure 5. Band structure of [111] SiNWs doped with B. Where, a, b, and c denote the substitution of the dopant at three different positions on [111] SiNWs structures.

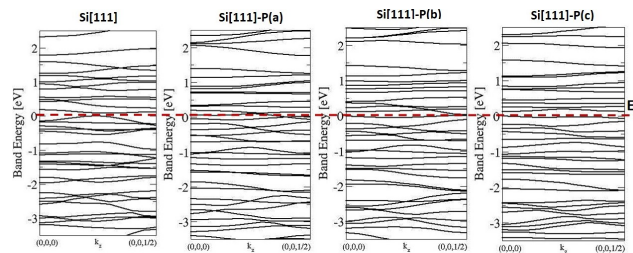


Figure 6. Band structure of [111] SiNWs doped with P. Where, a, b, and c denote the substitution of dopant at three different positions on [111] SiNWs structures.

Table 4. Energy gaps of [111] SiNWs and [111] SiNWs with doped with B and P.

	Band Gap (e.V)
SiNWs[111]	0.0852 direct band gap
SiNWs[111]-B(a)	0.102 indirect band gap
SiNWs[111]-B(b)	0.086
SiNWs[111]-B(c)	0.015
SiNWs[111]-P(a)	0.0 metallic
SiNWs[111]-P(b)	0.024
SiNWs[111]-P(c)	0.0 metallic

In the case of doping with B and P, we studied the influence of the radial distribution of the dopant by the substitution of three different positions for SiNWs structures that are shown in Figure 2—we denote them as a, b, and c. Position (a) and (b) are four-fold coordinated sites, which differ by symmetry, in particular after geometry optimization. Position (c) is under-coordinated, hence corresponds to doping in the SiNW surface.

For most doped structures, there are energy gap values of two types, direct and indirect, as indicated in Table 4. Doping SiNWs [111] with P in position (a) is an exception,

as there is no energy gap. This confirms the metallic nature of the latter wire type. In the case of passivated SiNWs [111] with hydrogen, the band gap is dependent on nanowire diameters; thus, the wires exhibited a transition from an indirect gap in large wires to a direct one in small wires [76].

As noted in earlier studies, SiNWs exhibit a size-dependent transition in their band gap characteristics. Larger SiNWs (diameters > 5 nm) retain an indirect band gap, akin to bulk silicon. As the wire diameter decreases to between 3–5 nm, the band gap begins to show mixed characteristics due to quantum confinement effects. When the diameter is further reduced to less than 3 nm, the band gap becomes direct, enhancing the wires potential for optoelectronic applications [76,77]. The direct band gap in small silicon nanowires (SiNWs) with diameters less than 3 nm makes them highly suitable for optoelectronic applications such as light-emitting devices and photo detectors, where efficient photon emission is crucial. This direct band gap allows for more efficient electron–hole recombination, enhancing their performance in these applications. Additionally, the transition from an indirect to a direct band gap significantly impacts the electronic properties of SiNWs. This change influences their electrical conductivity and enhances their potential for various semiconductor applications, providing greater versatility in the design and functionality of electronic devices [78].

We conclude that the actual electrical properties of SiNWs are strongly dependent on the growth directions and may be tuned by the chemical environment of the dangling bonds, as well as by the size, position and valence state of additional dopant atoms. These results confirm and substantially extend earlier findings obtained by David and Rurali et al. [68].

5. Conclusions

This study presents the impact of B and P doping on the electrical properties of SiNWs using a first-principles approach. The band dispersions in the [001] and [111] directions were compared with those of bulk silicon. It has been concluded that [001]-oriented SiNWs display a metallic property in the absence of passivation of surface dangling bonds, with either a negligible negative band gap or no band gap at all. It is further concluded that [111]-oriented SiNWs exhibit a direct band semiconductor behavior. Additionally, the influence of substituting boron and phosphorus atoms on the band structure of [001] and [111] SiNWs is examined, revealing significant impacts. The dangling bonds gives rise to the surface states. Saturating these states can cause shifts in the electrostatic potential and maybe used to tune the sensing properties of SiNWs.

Author Contributions: Validation, F.H.; Investigation, N.A.M.A.-N.; Writing—original draft, N.A.M.A.-N.; Writing—review & editing, N.A.M.A.-N. and S.G. All authors have read and agreed to the published version of the manuscript.

Funding: This research was funded by Deutsche Forschungsgemeinschaft grant number 405595647.

Data Availability Statement: The original contributions presented in the study are included in the article, further inquiries can be directed to the corresponding author.

Acknowledgments: This work was financially supported by the DFG via project number 405595647 and by providing compute time via project INST 270/290- 1 FUGB.

Conflicts of Interest: The authors declare no conflict of interest.

References

1. Georgiev, Y.M.; Petkov, N.; Yu, R.; Nightingale, A.M.; Buitrago, E.; Lotty, O.; deMello, J.C.; Ionescu, A.; Holmes, J.D. Detection of ultra-low protein concentrations with the simplest possible field effect transistor. *Nanotechnology* **2019**, *30*, 324001. [[CrossRef](#)] [[PubMed](#)]
2. Gupta, R.K. *Nanowires: Applications, Chemistry, Materials, and Technologies*; CRC Press: Boca Raton, FL, USA, 2023.
3. Nabet, B. *Photodetectors: Materials, Devices and Applications*; Woodhead Publishing: Sawston, UK, 2023.
4. Thomas, S.; Kalarikkal, N.; Abraham, A.R. *Applications of Multifunctional Nanomaterials*; Elsevier: Amsterdam, The Netherlands, 2023.
5. Singh, V.N. *Chemical Methods for Processing Nanomaterials*; CRC Press: Boca Raton, FL, USA, 2021.

6. Ng, M.F.; Zhou, L.; Yang, S.W.; Sim, L.Y.; Tan, V.B.; Wu, P. Theoretical investigation of silicon nanowires: Methodology, geometry, surface modification, and electrical conductivity using a multiscale approach. *Phys. Rev. B* **2007**, *76*, 155435. [[CrossRef](#)]
7. Jang, M.; Park, Y.; Jun, M.; Hyun, Y.; Choi, S.J.; Zyung, T. The characteristics of Seebeck coefficient in silicon nanowires manufactured by CMOS compatible process. *Nanoscale Res. Lett.* **2010**, *5*, 1654–1657. [[CrossRef](#)] [[PubMed](#)]
8. Stern, E.; Klemic, J.F.; Routenberg, D.A.; Wyrembak, P.N.; Turner-Evans, D.B.; Hamilton, A.D.; LaVan, D.A.; Fahmy, T.M.; Reed, M.A. Label-free immunodetection with CMOS-compatible semiconducting nanowires. *Nature* **2007**, *445*, 519–522. [[CrossRef](#)] [[PubMed](#)]
9. Cui, Y.; Lieber, C.M. Functional nanoscale electronic devices assembled using silicon nanowire building blocks. *Science* **2001**, *291*, 851–853. [[CrossRef](#)] [[PubMed](#)]
10. Alivisatos, P. The use of nanocrystals in biological detection. *Nat. Biotechnol.* **2004**, *22*, 47–52. [[CrossRef](#)] [[PubMed](#)]
11. Cui, Y.; Wei, Q.; Park, H.; Lieber, C.M. Nanowire nanosensors for highly sensitive and selective detection of biological and chemical species. *Science* **2001**, *293*, 1289–1292. [[CrossRef](#)] [[PubMed](#)]
12. Wang, W.U.; Chen, C.; Lin, K.H.; Fang, Y.; Lieber, C.M. Label-free detection of small-molecule–protein interactions by using nanowire nanosensors. *Proc. Natl. Acad. Sci. USA* **2005**, *102*, 3208–3212. [[CrossRef](#)] [[PubMed](#)]
13. Hahm, J.I.; Lieber, C.M. Direct ultrasensitive electrical detection of DNA and DNA sequence variations using nanowire nanosensors. *Nano Lett.* **2004**, *4*, 51–54. [[CrossRef](#)]
14. Patolsky, F.; Zheng, G.; Hayden, O.; Lakadamyali, M.; Zhuang, X.; Lieber, C.M. Electrical detection of single viruses. *Proc. Natl. Acad. Sci. USA* **2004**, *101*, 14017–14022. [[CrossRef](#)]
15. Zheng, G.; Patolsky, F.; Cui, Y.; Wang, W.U.; Lieber, C.M. Multiplexed electrical detection of cancer markers with nanowire sensor arrays. *Nat. Biotechnol.* **2005**, *23*, 1294–1301. [[CrossRef](#)] [[PubMed](#)]
16. Santana, J.E.; García, K.J.; De Santiago, F.; Miranda, Á.; Pérez-Figueroa, S.E.; González, J.E.; Pérez, L.A.; Cruz-Irisson, M. Selective sensing of DNA/RNA nucleobases by metal-functionalized silicon nanowires: A DFT approach. *Surfaces Interfaces* **2023**, *36*, 102529. [[CrossRef](#)]
17. Leu, P.W.; Shan, B.; Cho, K. Surface chemical control of the electronic structure of silicon nanowires: Density functional calculations. *Phys. Rev. B* **2006**, *73*, 195320. [[CrossRef](#)]
18. Guo, Z.; Arachchige, L.J.; Qiu, S.; Zhang, X.; Xu, Y.; Langford, S.J.; Sun, C. p-Block element-doped silicon nanowires for nitrogen reduction reaction: A DFT study. *Nanoscale* **2021**, *13*, 14935–14944. [[CrossRef](#)] [[PubMed](#)]
19. Cheng, B.; Deng, X.H.; Gu, X.; He, Y.; Hu, G.; Huang, P.; Li, J.; Lin, B.C.; Lu, D.; Lu, Y.; et al. Noisy intermediate-scale quantum computers. *Front. Phys.* **2023**, *18*, 21308.
20. Joseph, T.; Fuchs, F.; Schuster, J. Electronic structure simulation of thin silicon layers: Impact of orientation, confinement, and strain. *Phys. E Low-Dimens. Syst. Nanostruct.* **2023**, *146*, 115522. [[CrossRef](#)]
21. Lu, A.J.; Zhang, R.; Lee, S.T. Tunable electronic band structures of hydrogen-terminated [112] silicon nanowires. *Appl. Phys. Lett.* **2008**, *92*, 203109. [[CrossRef](#)]
22. Svizhenko, A.; Leu, P.W.; Cho, K. Effect of growth orientation and surface roughness on electron transport in silicon nanowires. *Phys. Rev. B* **2007**, *75*, 125417. [[CrossRef](#)]
23. Neophytou, N.; Paul, A.; Lundstrom, M.S.; Klimeck, G. Bandstructure effects in silicon nanowire electron transport. *IEEE Trans. Electron Devices* **2008**, *55*, 1286–1297. [[CrossRef](#)]
24. Ng, M.F.; Sullivan, M.B.; Tong, S.W.; Wu, P. First-principles study of silicon nanowire approaching the bulk limit. *Nano Lett.* **2011**, *11*, 4794–4799. [[CrossRef](#)]
25. Fuchs, F.; Gemming, S.; Schuster, J. Radially resolved electronic structure and charge carrier transport in silicon nanowires. *Phys. E Low-Dimens. Syst. Nanostruct.* **2019**, *108*, 181–186. [[CrossRef](#)]
26. Tran, F.; Blaha, P. Accurate band gaps of semiconductors and insulators with a semilocal exchange–correlation potential. *Phys. Rev. Lett.* **2009**, *102*, 226401. [[CrossRef](#)]
27. Ma, D.; Lee, C.; Au, F.; Tong, S.; Lee, S. Small-diameter silicon nanowire surfaces. *Science* **2003**, *299*, 1874–1877. [[CrossRef](#)] [[PubMed](#)]
28. Fuchs, F.; Khan, M.B.; Deb, D.; Pohl, D.; Schuster, J.; Weber, W.M.; Mühle, U.; Löffler, M.; Erbe, A.; Gemming, S. Formation and crystallographic orientation of NiSi₂–Si interfaces. *J. Appl. Phys.* **2020**, *128*, 085301. [[CrossRef](#)]
29. Holmes, J.D.; Johnston, K.P.; Doty, R.C.; Korgel, B.A. Control of thickness and orientation of solution-grown silicon nanowires. *Science* **2000**, *287*, 1471–1473. [[CrossRef](#)] [[PubMed](#)]
30. Wu, Y.; Cui, Y.; Huynh, L.; Barrelet, C.J.; Bell, D.C.; Lieber, C.M. Controlled growth and structures of molecular-scale silicon nanowires. *Nano Lett.* **2004**, *4*, 433–436. [[CrossRef](#)]
31. Gonze, X.; Amadon, B.; Anglade, P.M.; Beuken, J.M.; Bottin, F.; Boulanger, P.; Bruneval, F.; Caliste, D.; Caracas, R.; Côté, M.; et al. ABINIT: First-principles approach to material and nanosystem properties. *Comput. Phys. Commun.* **2009**, *180*, 2582–2615. [[CrossRef](#)]
32. Hochbaum, A.I.; Yang, P. Semiconductor nanowires for energy conversion. *Chem. Rev.* **2010**, *110*, 527–546. [[CrossRef](#)]
33. Wang, Q.; Meng, T.; Li, Y.; Yang, J.; Huang, B.; Ou, S.; Meng, C.; Zhang, S.; Tong, Y. Consecutive chemical bonds reconstructing surface structure of silicon anode for high-performance lithium-ion battery. *Energy Storage Mater.* **2021**, *39*, 354–364. [[CrossRef](#)]
34. Zhang, F.; Zhu, W.; Li, T.; Yuan, Y.; Yin, J.; Jiang, J.; Yang, L. Advances of synthesis methods for porous silicon-based anode materials. *Front. Chem.* **2022**, *10*, 889563. [[CrossRef](#)]

35. Cui, Y.; Duan, X.; Hu, J.; Lieber, C.M. Doping and electrical transport in silicon nanowires. *J. Phys. Chem. B* **2000**, *104*, 5213–5216. [[CrossRef](#)]
36. Ma, D.; Lee, C.; Lee, S. Scanning tunneling microscopic study of boron-doped silicon nanowires. *Appl. Phys. Lett.* **2001**, *79*, 2468–2470. [[CrossRef](#)]
37. Sharma, D.; Fagas, G. A study of atomic orbital basis sets for doped silicon nanowires. In *Proceedings of the Journal of Physics: Conference Series*; IOP Publishing: Bristol, USA, 2012; Volume 367, p. 012003.
38. Ng, M.F.; Tong, S.W. Chemically doped radial junction characteristics in silicon nanowires. *Nano Lett.* **2012**, *12*, 6133–6138. [[CrossRef](#)]
39. Fukata, N. Impurity doping in silicon nanowires. *Adv. Mater.* **2009**, *21*, 2829–2832. [[CrossRef](#)]
40. Fujii, M.; Yamaguchi, Y.; Takase, Y.; Ninomiya, K.; Hayashi, S. Control of photoluminescence properties of Si nanocrystals by simultaneously doping n-and p-type impurities. *Appl. Phys. Lett.* **2004**, *85*, 1158–1160. [[CrossRef](#)]
41. Ghosh, S.; Chava, P.; Watanabe, K.; Taniguchi, T.; Prucnal, S.; Hübner, R.; Mikolajick, T.; Erbe, A.; Georgiev, Y.M. Novel Mixed-Dimensional hBN-Passivated Silicon Nanowire Reconfigurable Field Effect Transistors: Fabrication and Characterization. *ACS Appl. Mater. Interfaces* **2023**, *15*, 40709. [[CrossRef](#)]
42. König, D.; Hiller, D.; Gutsch, S.; Zacharias, M.; Smith, S. Modulation Doping of Silicon using Aluminium-induced Acceptor States in Silicon Dioxide. *Sci. Rep.* **2017**, *7*, 46703. [[CrossRef](#)]
43. Pang, Q.; Zahng, J.M.; Zhang, Y.; Ji, V.; Xu, K.W. Properties of the bare, passivated and doped germanium nanowire: A density-functional theory study. *Comp. Mater. Sci.* **2010**, *49*, 682. [[CrossRef](#)]
44. Masoumifard, Raheleand Oftadeh, M.; Eskandari, K. Investigation of Quantum Conductance in Silicon Nanowire Doped with Boron in the Presence and Absence of (3-Aminopropyl) Triethoxysilane Molecule. *Iran. J. Sci.* **2023**, *47*, 1145–1154. [[CrossRef](#)]
45. Gueorguiev, G.K.; Stafström, S.; Hultman, L. Nano-wire formation by self-assembly of silicon–metal cage-like molecules. *Chem. Phys. Lett.* **2008**, *458*, 170–174. [[CrossRef](#)]
46. Oliveira, M.; Rivelino, R.; de Brito Mota, F.; Gueorguiev, G.K. Optical properties and quasiparticle band gaps of transition-metal atoms encapsulated by silicon cages. *J. Phys. Chem. C* **2014**, *118*, 5501–5509. [[CrossRef](#)]
47. Momma, K.; Izumi, F. VESTA 3 for three-dimensional visualization of crystal, volumetric, and morphology data. *J. Appl. Crystallogr.* **2011**, *44*, 1272–1276. [[CrossRef](#)]
48. Kaduk, J. Crystallographic databases and powder diffraction. *Int. Tables Crystallogr.* **2019**, *H*, 304.
49. Hohenberg, P.; Kohn, W. Density functional theory (DFT). *Phys. Rev.* **1964**, *136*, B864. [[CrossRef](#)]
50. Kohn, W.; Sham, L.J. Self-consistent equations including exchange and correlation effects. *Phys. Rev.* **1965**, *140*, A1133. [[CrossRef](#)]
51. Gonze, X.; Beuken, J.M.; Caracas, R.; Detraux, F.; Fuchs, M.; Rignanese, G.M.; Sindic, L.; Verstraete, M.; Zerah, G.; Jollet, F.; et al. First-principles computation of material properties: The ABINIT software project. *Comput. Mater. Sci.* **2002**, *25*, 478–492. [[CrossRef](#)]
52. Nolan, M.; O’Callaghan, S.; Fagas, G.; Greer, J.C.; Frauenheim, T. Silicon nanowire band gap modification. *Nano Lett.* **2007**, *7*, 34–38. [[CrossRef](#)] [[PubMed](#)]
53. Khan, M.B.; Deb, D.; Kerbusch, J.; Fuchs, F.; Löffler, M.; Banerjee, S.; Mühle, U.; Weber, W.M.; Gemming, S.; Schuster, J.; et al. Towards Reconfigurable Electronics: Silicidation of Top-Down Fabricated Silicon Nanowires. *Appl. Sci.* **2019**, *9*, 3462. [[CrossRef](#)]
54. Miranda, A.; De Santiago, F.; Pérez, L.; Cruz-Irisson, M. Silicon nanowires as potential gas sensors: A density functional study. *Sens. Actuators B Chem.* **2017**, *242*, 1246–1250. [[CrossRef](#)]
55. Perdew, J.P.; Burke, K.; Ernzerhof, M. Generalized gradient approximation made simple. *Phys. Rev. Lett.* **1996**, *77*, 3865. [[CrossRef](#)] [[PubMed](#)]
56. Lejaeghere, K.; Bihlmayer, G.; Björkman, T.; Blaha, P.; Blügel, S.; Blum, V.; Caliste, D.; Castelli, I.E.; Clark, S.J.; Dal Corso, A.; et al. Reproducibility in density functional theory calculations of solids. *Science* **2016**, *351*, aad3000. [[CrossRef](#)] [[PubMed](#)]
57. Zhang, Y.; Yang, W. Comment on “Generalized gradient approximation made simple”. *Phys. Rev. Lett.* **1998**, *80*, 890. [[CrossRef](#)]
58. Hammer, B.; Hansen, L.B.; Nørskov, J.K. Improved adsorption energetics within density-functional theory using revised Perdew-Burke-Ernzerhof functionals. *Phys. Rev. B* **1999**, *59*, 7413. [[CrossRef](#)]
59. Gonze, X.; Jollet, F.; Araujo, F.A.; Adams, D.; Amadon, B.; Applencourt, T.; Audouze, C.; Beuken, J.M.; Bieder, J.; Bokhanchuk, A.; et al. Recent developments in the ABINIT software package. *Comput. Phys. Commun.* **2016**, *205*, 106–131. [[CrossRef](#)]
60. Malica, C.; Dal Corso, A. Quasi-harmonic temperature-dependent elastic constants: Applications to silicon, aluminum, and silver. *J. Physics Condens. Matter* **2020**, *32*, 315902. [[CrossRef](#)] [[PubMed](#)]
61. Nielsen, O.; Martin, R.M. Stresses in semiconductors: Ab initio calculations on Si, Ge, and GaAs. *Phys. Rev. B* **1985**, *32*, 3792. [[CrossRef](#)]
62. Zhao, J.; Winey, J.; Gupta, Y. First-principles calculations of second-and third-order elastic constants for single crystals of arbitrary symmetry. *Phys. Rev. B* **2007**, *75*, 094105. [[CrossRef](#)]
63. Råsander, M.; Moram, M. On the accuracy of commonly used density functional approximations in determining the elastic constants of insulators and semiconductors. *J. Chem. Phys.* **2015**, *143*. [[CrossRef](#)]
64. McSkimin, H. Measurement of elastic constants at low temperatures by means of ultrasonic waves—data for silicon and germanium single crystals, and for fused silica. *J. Appl. Phys.* **1953**, *24*, 988–997. [[CrossRef](#)]
65. Ashcroft, N.W. Solid State Physics (HR&W) Google Scholar NW Ashcroft and ND Mermin 1979. *Solid State Phys.* **1976**, *1*, 2.

66. Kumarasinghe, C.; Bowler, D.R. DFT study of undoped and As-doped Si nanowires approaching the bulk limit. *J. Phys. Condens. Matter* **2019**, *32*, 035304. [[CrossRef](#)] [[PubMed](#)]
67. Mukhanov, V.A.; Courac, A.; Solozhenko, V.L. The effect of doping on the lattice parameter and properties of cubic boron nitride. *J. Superhard Mater.* **2020**, *42*, 377–387. [[CrossRef](#)]
68. Dass, D. Metallic-semiconducting transition of silicon nanowires by surface passivation. *Results Surfaces Interfaces* **2021**, *3*, 100009. [[CrossRef](#)]
69. Rurali, R. Colloquium: Structural, electronic, and transport properties of silicon nanowires. *Rev. Mod. Phys.* **2010**, *82*, 427. [[CrossRef](#)]
70. Ramstad, A.; Brocks, G.; Kelly, P. Theoretical study of the Si (100) surface reconstruction. *Phys. Rev. B* **1995**, *51*, 14504. [[CrossRef](#)] [[PubMed](#)]
71. Rurali, R.; Lorente, N. Metallic and semimetallic silicon< 100> nanowires. *Phys. Rev. Lett.* **2005**, *94*, 026805.
72. Durgun, E.; Akman, N.; Ataca, C.; Ciraci, S. Atomic and electronic structures of doped silicon nanowires: A first-principles study. *Phys. Rev. B* **2007**, *76*, 245323. [[CrossRef](#)]
73. Durgun, E.; Akman, N.; Ciraci, S. Functionalization of silicon nanowires with transition metal atoms. *Phys. Rev. B* **2008**, *78*, 195116. [[CrossRef](#)]
74. Chien, P.J.; Wei, T.C.; Chen, C.Y. High-speed and direction-controlled formation of silicon nanowire arrays assisted by electric field. *Nanoscale Res. Lett.* **2020**, *15*, 25. [[CrossRef](#)]
75. Leu, P.W.; Svizhenko, A.; Cho, K. Ab initio calculations of the mechanical and electronic properties of strained Si nanowires. *Phys. Rev. B* **2008**, *77*, 235305. [[CrossRef](#)]
76. Zhao, X.; Wei, C.; Yang, L.; Chou, M. Quantum confinement and electronic properties of silicon nanowires. *Phys. Rev. Lett.* **2004**, *92*, 236805. [[CrossRef](#)] [[PubMed](#)]
77. Delley, B.; Steigmeier, E. Size dependence of band gaps in silicon nanostructures. *Appl. Phys. Lett.* **1995**, *67*, 2370–2372. [[CrossRef](#)]
78. Barbagiovanni, E.G.; Lockwood, D.J.; Simpson, P.J.; Goncharova, L.V. Quantum confinement in Si and Ge nanostructures: Theory and experiment. *Appl. Phys. Rev.* **2014**, *1*, 011302. [[CrossRef](#)]

Disclaimer/Publisher’s Note: The statements, opinions and data contained in all publications are solely those of the individual author(s) and contributor(s) and not of MDPI and/or the editor(s). MDPI and/or the editor(s) disclaim responsibility for any injury to people or property resulting from any ideas, methods, instructions or products referred to in the content.